J Mater Sci (2012) 47:929–948
DOI 10.1007/s10853-011-5873-1

Prediction of hot deformation behavior of Al–5.9%Cu–0.5%Mg alloys with trace additions of Sn

Sanjib Banerjee · P. S. Robi · A. Srinivasan

Received: 11 May 2011 / Accepted: 11 August 2011 / Published online: 25 August 2011

Abstract High temperature deformation behavior of Al–5.9wt%Cu–0.5wt%Mg alloys containing trace amounts (from 0 to 0.1 wt%) of Sn was studied by hot compression tests conducted at various temperatures and strain rates. The peak flow stress of the alloys increased with increase in strain rate and decrease in deformation temperature. The peak stress could be correlated with temperature and strain rate by a suitable hyperbolic-sine constitutive equation. The activation energy for hot deformation of the alloy without Sn content was observed to be 183.4 kJ mol^{-1} which increased to 225.5 kJ mol^{-1} due to 0.08 wt% of Sn addition. The Zener-Hollomon parameter (Z) was determined at various deforming conditions. The tendency of dynamic recrystallization increased with low Z values, corresponding to low strain rate and high temperature. The peak flow stresses at various processing conditions have been predicted by the constitutive modeling and correlated with the experimental results with fairly good accuracy. It was possible to predict 80, 75, 100, 100, 90, and 85% of the peak stress values within an error less than ±13%, for the investigated alloys. With addition of Sn content >0.04 wt%, peak flow stress increased significantly for all strain rate and temperature combinations. Scanning electron microscope revealed two types of second phases at the grain boundary of the undeformed alloy matrix, one being an Al–Cu–Si–Fe–Mn phase while the other identified as $CuAl_2$. The high strength and flow stress value of the alloy with 0.06 wt% of Sn content, may be attributed to the variation in amount, composition, and morphology of the Al–Cu–Si–Fe–Mn phase, as well as to the lower value of activation energy for precipitation reaction, as revealed from differential scanning calorimetric studies.

S. Banerjee (✉)
Department of Mechanical Engineering, Tezpur University, 784028 Tezpur, India
e-mail: sanjibb@iitg.ernet.in

P. S. Robi
Department of Mechanical Engineering, Indian Institute of Technology Guwahati, 781039 Guwahati, India

A. Srinivasan
Department of Physics, Indian Institute of Technology Guwahati, 781039 Guwahati, India

Introduction

The high demand and interest in aircraft- and space-related applications in the recent years have resulted in a thrust in development of light weight alloys exhibiting better mechanical properties. Several decades of intense research work has focused in the development of such alloys having high specific strength, reasonable ductility, high fracture toughness, and good corrosion resistance properties [1, 2]. The high density and comparatively poor electrical and thermal conductivity compared to many non-ferrous alloys restrict the use of ferrous alloys in these aircraft and space applications. The focus therefore was specifically on the alloys of aluminum, titanium, magnesium, etc. Out of these entire alloy systems, aluminum alloys, especially the wrought and precipitation strengthened Al–Cu (2xxx), Al–Mg–Si (6xxx), and Al–Zn–Mg–Cu (7xxx) series of alloys were developed because of their high strength to weight ratio. The 2xxx series of Al alloys are used for high strength structural applications such as aircraft fittings and wheels, rocket fins, military vehicles and bridges, forgings for trucks, etc. The Al–Cu–Mg alloys of 2124, 2219, and 2618 are extensively being used in aerospace structures demanding good heat resistance properties up to 150 °C

[3–6]. These are wrought alloys and are generally used after deformation processing followed by a sequence of heat treatments.

The mechanisms of strengthening and toughening of these materials are now fairly established [2]. The mechanical properties of these alloys are affected by the composition, strain history, and the microstructure resulting from the thermo-mechanical treatment imparted before the final use. On the other hand, the mechanical properties are also affected even by minute variations in the composition and microstructure of the alloys. The present research trend to develop these materials with increased strength combined with properties of reasonable toughness and low density is by the addition of trace elements (microalloying, i.e., alloying elements <0.1 wt%) like Sn, In, Cd, Ag, Si, etc., into the alloy matrix [7–12].

The wrought alloys for structural application need to undergo a thermo-mechanical treatment prior to their final use. These alloys are required to be plastically deformed to reduce the defects (viz., segregations, dendrite structures, gas defects, inclusions, etc.) induced during casting. The deformation process is generally carried out at high homologous temperatures, i.e., $T/T_m > 0.5$, where T and T_m are the absolute working temperature and melting temperature of the material, respectively. In high temperature deformation, the two main research areas are (i) creep deformation and (ii) metal forming by hot working. The major objectives in hot working are to reduce the flow stress and raise the fracture strain at high strain rates ($10^{-2}\ s^{-1} < \dot{\varepsilon} < 10^{2}\ s^{-1}$), whereas the emphasis in creep research is for low strain rates and curtailment of total strain, even though both these studies are carried out at almost the same temperature range [13, 14]. A clear understanding of the process variables and material parameters is required for successfully deforming these materials within a range of strain rates and temperatures. The deformation behavior of these materials, i.e., the relationship between flow stress (σ), strain (ε), strain rate ($\dot{\varepsilon}$), and processing temperature (T) is dependent on the activation energy (Q) for deformation, which is a measure of the degree of hindrance to deformation. Composition and microstructure strongly influence the Q value of the materials. Considering hot deformation similar to the creep phenomenon occurring at high strain rates and stresses [15], various constitutive relationships have been developed to model the high temperature deformation behavior of the materials. These investigations show that the flow stress can also be represented by a Zener-Hollomon parameter, Z.

A thermo-viscoplastic finite element method (FEM) was developed using hot compression test data to predict the microstructural evolution in Al–5wt%Mg alloys during hot deformation [16]. Based on experimental results, a unified creep-plasticity constitutive model for the stress–strain behavior of cast Al–Cu–Si alloys under complex loading conditions has been proposed [17]. Kaibyshev et al. [18] investigated the deformation behavior of a 2219 Al alloy (Al–6.4%Cu–0.3%Mn–0.18%Cr–0.19%Zr–0.06%Fe) in the temperature range from 250 to 500 °C, which is the widely used hot working temperature range for this alloy. The results indicated an increase in stress exponent and apparent activation energy with decrease in T. A power law equation was used for modeling the variation of flow stress with $\dot{\varepsilon}$. The value of the energy term, Q, was evaluated as 35 kJ mol^{-1} in the T range of 250 to 450 °C, which decreased at higher T. Deformation behavior of this 2219 Al alloy indicated the presence of a threshold stress which was found to be temperature dependent. Microstructural studies of this alloy also revealed localization of dislocation glide with decrease in T and increase in $\dot{\varepsilon}$. On the other hand, an increase in T resulted in possible cross-slip and a transition from multiple slip to single slip. Superplastic deformation behavior of the same alloy has also been studied [19]. Thermo-mechanical processing was necessary for obtaining the appropriate microstructure (viz., large secondary particles of size $\sim$1 μm), favorable for superplastic deformation of the alloy. The alloy exhibited a maximum strain of 675% at 500 °C with an initial grain size of 12 μm and a constant $\dot{\varepsilon}$ of $2.2 \times 10^{-4}\ s^{-1}$.

Hot and warm formability studies on as-solutionized 2618 Al alloy (Al–2.3%Cu–1.6%Mg–1.1%Fe–1.0%Ni–0.07%Ti–0.18%Si) at various strain rates and temperatures by torsion testing revealed precipitation of second phase particles during deformation [20]. The flow curves showed a temperature-dependent behavior with (i) a continuous increase of flow stress up to 250 °C due to precipitation and (ii) a peak in the flow curves above 250 °C due to precipitation and coarsening of precipitates followed by softening. The high temperature tensile deformation behavior of Al–Cu–Mg–Zr alloy, 2014, and 6082 Al alloys in a wide range of T and $\dot{\varepsilon}$ were described by a modified hyperbolic-sine equation, where the peak flow stress (σ_p) was substituted by an effective stress, i.e., the difference between peak stress and a threshold stress representing the strengthening effect of the second phase precipitates in the matrix [21, 22]. Flow stress behaviors of Al–Cu–Li–Zr, Al–Mg, Al–Cu–Mg–Ag, and Al–Mg–Si–Cu alloys have been studied extensively [15, 23–25] by hot compression tests. These studies indicated that the plastic deformation of these alloys at elevated temperatures ($T > 0.5T_m$) is a thermally activated process with an activation energy Q. The flow stress has either an exponential or hyperbolic-sine relationship with $\dot{\varepsilon}$ and T.

Research so far, was focused on determining the Zener-Hollomon parameter, activation energy and various other constants in the constitutive models describing the hot

deformation behavior of some commercially available aluminum alloys. These may be affected even by minute variations in composition and microstructure of the alloys, and subsequently the mechanical properties are thus greatly enhanced by microalloying with elements like silver, tin, indium, scandium, etc. Although constitutive analysis have been reported on the high temperature deformation behavior of some commercial aluminum alloys, investigations on the effect of microalloying on the hot deformation behavior of highly applicable wrought 2xxx series of aluminum alloys are still very rare.

The purpose of the present study is therefore to investigate the influence of trace additions of tin (Sn) on the high temperature deformation/flow behavior of Al–Cu–Mg alloys. Selecting elemental Sn becomes a worthy of investigation since Sn has already been reported to affect the mechanical properties of some Al alloys [8]. The deformation behavior of Al–5.9wt%Cu–0.5wt%Mg alloys with systematic variation in Sn content (ranging from 0 to 0.1 wt%) were studied by hot compression tests performed at various processing temperatures and strain rates. The constitutive equations correlating peak flow stress, deformation temperature, strain rate, Zener-Hollomon parameter, and activation energy for deformation were generated for the alloys. The peak flow stresses (σ_p), predicted by the respective constitutive analysis were successfully compared with the experimental results. The present work is an attempt made to develop the parameters of the constitutive model, of highly applicable wrought 2xxx series of Al–Cu–Mg alloys microalloyed with systematic variations in Sn content, and thereby to predict the peak flow stress value of these materials. Microstructural analysis was also performed in support of the variation in peak stress value with trace additions of Sn.

Experimental procedures

Al–Cu–Mg and Al–Cu–Mg–Sn alloys were prepared from aluminum ingots of commercial purity by a casting route. The base alloy (Alloy-*A*) was chosen to have a composition of Al–5.9%Cu–0.5%Mg (by weight), which is close to the 2219Al alloy. Alloy-*B* to Alloy-*F* correspond to the base alloy microalloyed with 0.02 to 0.1 wt% of Sn. The alloys were thus designated as Alloy-*A* to Alloy-*F* based on their Sn contents as shown in Table 1.

The cylindrical samples cast in graphite molds were machined to 12 mm diameter and 200 mm length. The machined sample rods were then homogenized at 510 °C for 10 h to reduce the non-homogeneity in composition and microstructure resulting from coring and segregation during solidification. Cylindrical specimens having dimensions of 10 mm diameter and 15 mm height were then machined from the annealed rods for hot compression testing. Concentric grooves of 0.5 mm depth were machined on the top and bottom parallel surfaces of the specimens to retain the solid lubricant thereby reducing the friction at the sample–compression platen interface during the test. A hole of 1 mm diameter was drilled at the mid-height region of the sample for introducing the thermocouple to measure the temperature during the compression test.

Table 1 Designations of the alloys prepared

Sl no.	Alloy designation	Sn content (wt%)
1	Alloy-*A* (base alloy)	0.00
2	Alloy-*B*	0.02
3	Alloy-*C*	0.04
4	Alloy-*D*	0.06
5	Alloy-*E*	0.08
6	Alloy-*F*	0.10

High temperature compression tests were carried out using a servo-hydraulic controlled dynamic 100 kN capacity universal testing machine (UTM; INSTRON, Model 8801). A split-type resistance heated furnace was fabricated and attached to the UTM to maintain a constant test temperature. Machined and heat treated H-13 die steel compression platens were fabricated and used for the test. The platens were water jacketed to prevent transfer of heat to the UTM cross-head. The compression platens attached to the UTM were held inside the furnace and the specimen was placed between the platens. To reduce the friction during the compression testing, MoS_2 paste was applied at the work piece–compression platen interface. The sample temperature was raised at a rate of 5 °C s^{-1} to the required testing temperature. After attaining the test temperature, the sample temperature was maintained with an accuracy of ±3 °C for 15 min to ensure homogeneous temperature throughout the entire sample volume prior to the compression test.

The cross-head velocity of the UTM actuator was varied such that a constant true strain rate was maintained during the entire duration of the compression test using the relation [26]:

$$v = \dot{\varepsilon} L_o \exp(\dot{\varepsilon} t) \quad (1)$$

where v is the cross-head velocity, $\dot{\varepsilon}$ is the true strain rate, L_o is the initial specimen length, and t is the time elapsed. The actuator displacement at any instant of time was controlled by the closed loop servo-hydraulic control of the UTM and MAX^{TM} software was used for controlling the actuator movement. A computer code was generated to carry out the tests at different constant true strain rates, ($\dot{\varepsilon}$).

The strain rates ($\dot{\varepsilon}$) and temperatures (T), at which the tests were performed, are given in Table 2. The tests were carried out up to a true strain (ε) of 0.6. The load versus

Table 2 Strain rates and temperatures of the hot compression tests

$\dot{\varepsilon}$ (s^{-1})	T (°C)
0.001, 0.01, 0.1, and 1.0	300, 350, 400, 450, and 500

displacement plots for all the tests were obtained during the compression tests, from which the true stress (σ) versus true strain (ε) curves were obtained. The peak flow stresses for each combination of strain rate and temperature were determined from the plots. The Q and other parameters of the constitutive model defining the high temperature deformation behavior of the investigated alloys were then evaluated.

To observe the dynamic recrystallization (DRX) behavior, the microstructures of both undeformed as well as specimens deformed to a ε of 0.6 under various $\dot{\varepsilon}$ and T were observed using optical microscope (OM). Samples were prepared by standard metallographic technique. The polished and etched specimens were observed under an upright OM (Carl Ziess, Axiotech) equipped with Kontron KS-400 image analysis system. The grain size of the undeformed homogenized sample was determined by the standard line intercept method.

For further revealing of the undeformed microstructural details and various phases present, the respective polished (unetched) samples were gold coated using a sputter coater and observed under a scanning electron microscope (SEM, LEO, 1430 VP), under an accelerating voltage range of 10–20 kV. Images were observed under both secondary electron (SE) mode as well as back-scattered detector (BSD) image mode. The compositions of different phases present were analyzed using an energy dispersive X-ray spectrometer (EDS, Oxford) attached to the SEM. The EDS analysis was carried out using high purity cobalt as the reference standard and maintaining a working distance of 15 mm.

The kinetics of the precipitation and dissolution reactions observed during heat treatment of the Al–Cu–Mg alloys microalloyed with varying percentage of Sn were studied using a differential scanning calorimeter (DSC, Perkin Elmer, DSC 7). Four sets of samples were prepared from each alloy so as to carry out the experiments at four different heating rates. Samples were prepared in the form of discs of 3 mm diameter with weights in the range of 18–20 mg. The discs were vacuum encapsulated (at $\sim 10^{-3}$ Pa) in fused silica tubes and solutionized at 500 °C for 10 h followed by water quench to room temperature. The baseline data for each heating rate was recorded using high purity Al pan as the reference. DSC curves were recorded from 50 to 550 °C under a constant heating rate and then subsequently cooled to 50 °C at the same rate. Heating rates of 10, 15, 20, and 25 °C min^{-1} were used to obtain information on the kinetics of the reactions. High purity dry nitrogen atmosphere was maintained during the DSC runs to prevent oxidation of the samples. The reaction peaks obtained during the heating cycle were analyzed. The characteristic temperatures (onset, peak, and end) corresponding to the precipitation reactions were determined from the DSC curves.

An exothermic peak was observed in the temperature range of 200 to 300 °C in the DSC curves of the solutionized and quenched alloy samples. In order to understand the structural changes accompanying these exothermic reactions, XRD studies were carried out on the samples after appropriate heat treatment. XRD studies were performed on three different alloy compositions with Sn wt% of 0, 0.06, and 0.1. Samples of 10 mm × 10 mm size were sectioned and solutionized at 500 °C followed by water quenching. After the solutionizing heat treatment, one set of the samples was further annealed at 350 °C for 10 h. This annealing temperature was selected since the exothermic reaction was observed to be complete within this temperature, as revealed from the DSC thermograms. A commercial powder X-ray diffractometer (Seifert XRD 3003 T/T) was used for the phase identification in the alloys at room temperature. Cu K_α radiation (1.541 Å) with nickel filter was used. XRD patterns were recorded over a 2θ range of 5° to 70° (where θ is the glancing angle) with a scan rate of 0.05°/s. The possible phase(s) present in the heat-treated samples was (were) identified by comparing the peak position and intensity with data in the powder diffraction files available in ICPD database.

Results and discussion

Flow stress behavior

The flow curves (σ vs. ε plots) were obtained for the investigated alloys at various strain rates ($\dot{\varepsilon}$) and deformation temperatures (T). These curves for Alloy-*A*, Alloy-*C*, and Alloy-*F* are shown in Figs. 1, 2, and 3, respectively. The curves indicate strain-hardening behavior during plastic deformation. At the onset of plastic deformation, flow stress (σ) increased rapidly. The σ increased at a decreasing rate with increase in ε up to a maximum stress (σ_p). Beyond the peak strain (ε_p), i.e., the ε to reach the maximum stress, the σ either decreased with increase in ε or attained saturation. The former behavior is observed when the softening rate is higher than the work hardening rate, while the latter phenomenon occurs when the softening rate is equal to the work hardening rate [20, 24, 27, 28]. Flow softening after attaining the peak stress was observed in all the alloys at low $\dot{\varepsilon}$ of 0.001 s^{-1}. Undulations were observed at low $\dot{\varepsilon}$ in the flow curves beyond the

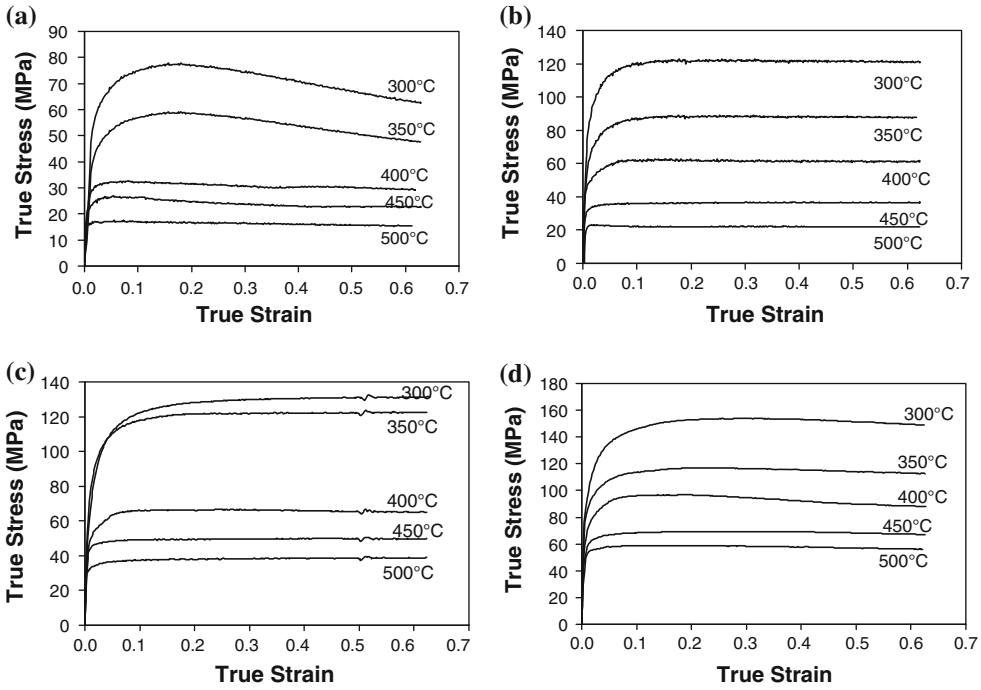

Fig. 1 Flow curves of Alloy-*A* at strain rates of **a** 0.001 s^{-1}, **b** 0.01 s^{-1}, **c** 0.1 s^{-1}, and **d** 1.0 s^{-1}

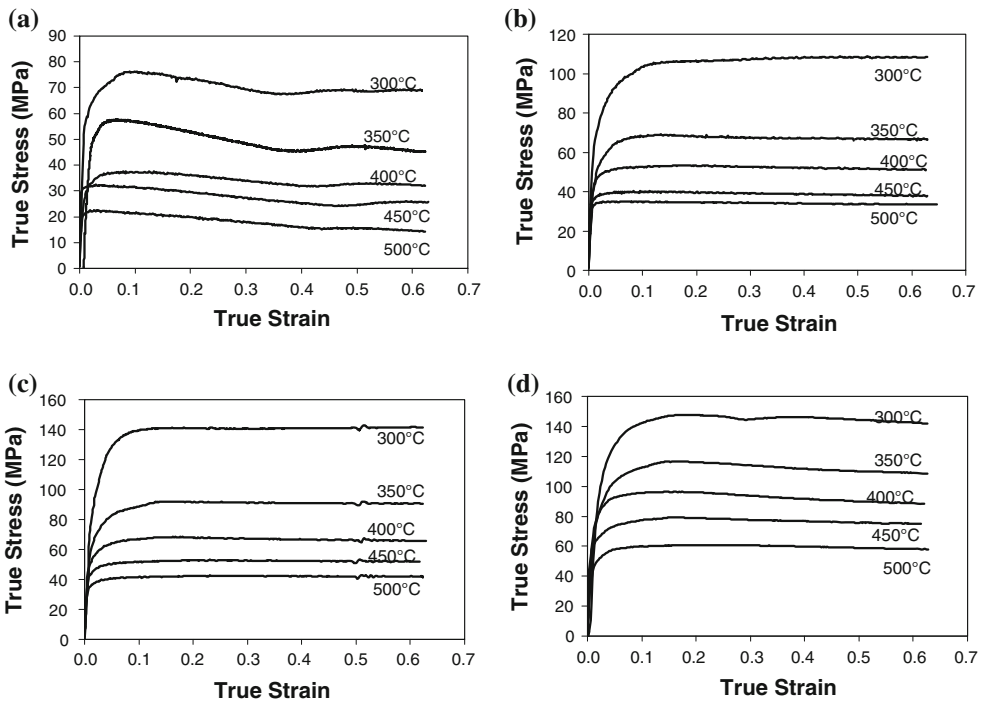

Fig. 2 Flow curves of Alloy-*C* at strain rates of **a** 0.001 s^{-1}, **b** 0.01 s^{-1}, **c** 0.1 s^{-1}, and **d** 1.0 s^{-1}

ε_p in all alloys microalloyed with Sn. These undulations persist up to 450 °C in the alloys containing Sn, the only exception being the alloy with 0.06 wt% Sn in which the undulations were not observed beyond 350 °C.

It is also evident that at a given temperature the peak flow stress (σ_p) increased with increase in strain rate, while at a given strain rate, higher the deformation temperature, lower was the σ_p value. These observations are in general agreement with earlier reports on metallic alloys [24, 25, 28–30]. Therefore the peak flow stress was highest for the investigated alloys deformed at 300 °C and strain rate of 1.0 s^{-1}, which decreased with increase in temperature and decrease in strain rate value.

For most of the combinations of $\dot{\varepsilon}$and T, no significant variation could be observed in the σ_p value of the investigated Al–Cu–Mg alloy system with increase in Sn content

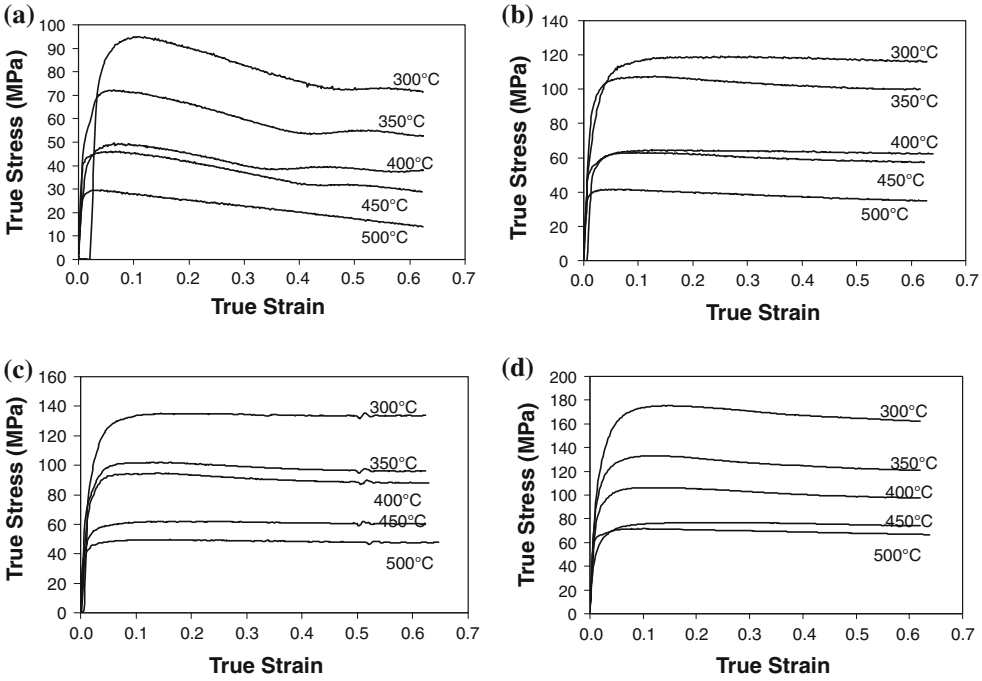

Fig. 3 Flow curves of Alloy-*F* at strain rates of **a** 0.001 s^{-1}, **b** 0.01 s^{-1}, **c** 0.1 s^{-1}, and **d** 1.0 s^{-1}

from 0 to 0.04 wt%. However, with further increase in Sn content up to 0.08 wt%, σ_p value increased abruptly for all $\dot{\varepsilon}$and T combinations. In case of 11 out of 20 deforming conditions, the peak flow stress of the base alloy increased due to increase in Sn content up to 0.04 wt%. It is worthy to mention that this increase was observed only at higher $T \geq 400$ °C. For the remaining cases, however, at the lower T ranges, the σ_p value decreased from Alloy-*A* to Alloy-*C*. But all these variations were not very significant in most of the cases or the peak stress values were observed to be quite comparable with the base alloy up to the Sn content of 0.04 wt%. While on the other hand, the σ_p value increased significantly with further additions of Sn above 0.04 wt%. For almost all the combinations of $\dot{\varepsilon}$and T, the peak flow stress of the Al–Cu–Mg alloy with 0.08 wt% of Sn (Alloy-*E*) was observed to be significantly higher than the respective values of all the remaining alloys investigated. At a $\dot{\varepsilon}$ of 0.001 s^{-1} and T of 300 °C, the σ_p of the base alloy (Alloy-*A*) increased by 40.8% due to trace additions of 0.08 wt% of Sn. When the $\dot{\varepsilon}$ was increased to 1.0 s^{-1} at the same T, the corresponding increase in peak flow stress was observed to be 23.8%. At the higher processing temperature of 500 °C, the corresponding increases in σ_p of Alloy-*A* due to 0.08 wt% of Sn addition were 105.1 and 18.7% for strain rates of 0.001 and 1.0 s^{-1}, respectively. Moreover, as revealed from the flow curves, even for various true strain (ε) values during the hot deformation process, the flow stress (σ) was observed to be higher in case of Alloy-*D* and Alloy-*E* compared to the respective values of the other investigated alloys.

Constitutive analysis

Considering hot deformation similar to the creep phenomenon, but occurring at high strain rates and stresses, various constitutive relationships have been developed to model the high temperature deformation behavior of materials. The strain rate ($\dot{\varepsilon}$) is related to the deformation temperature (T) and activation energy for deformation by the Arrhenius equation expressed as [15, 31]:

$$\dot{\varepsilon} = Af(\sigma)\exp\left(-\frac{Q}{RT}\right) \tag{2}$$

where, Q is the activation energy for deformation (J mol^{-1}), R is the universal gas constant (= 8.314 J mol^{-1} K^{-1}), T is the absolute working temperature (K), A is a constant, and $f(\sigma)$ is the stress function which can be expressed by any of the following equations [15, 24, 25, 28, 30, 32, 33]:

$$f(\sigma) = \sigma^{n_1} \tag{3}$$

$$f(\sigma) = \exp(\beta\sigma) \tag{4}$$

$$f(\sigma) = [\sinh(\alpha\sigma)]^n \tag{5}$$

Combining Eq. 2 with Eqs. 3–5, the following constitutive equations can be obtained:

$$\dot{\varepsilon} = A_1\sigma^{n_1}\exp\left(-\frac{Q}{RT}\right) \tag{6}$$

$$\dot{\varepsilon} = A_2\exp(\beta\sigma)\exp\left(-\frac{Q}{RT}\right) \tag{7}$$

$$\dot{\varepsilon} = A_3 \left[\sinh(\alpha\sigma)\right]^n \exp\left(-\frac{Q}{RT}\right) \quad (8)$$

In the above equations, though σ is generally taken as the peak flow stress (σ_p) [13, 27], the steady state flow stress (σ_s) has also been used in a few instances. It has been observed in many cases that σ_p and σ_s hold a linear relationship. The term α is the stress multiplier used in the mathematical fitting procedure. The terms of n_1, β, n, A_1, A_2, and A_3 are material constants.

The power law equation (Eq. 6) breaks down at high stress values whereas the exponential equation (Eq. 7) breaks down at low stress values [13, 15, 25, 27, 30, 33]. Over a wide range of stresses, the hyperbolic-sine law (Eq. 8) has been found to be the most suitable form for describing high temperature deformation behavior of materials.

For the present investigation, peak flow stress, σ_p, has been taken for the σ term in the above expressions. Determination of the value of stress multiplier α is very important for this analysis. No single solution exists for α and its value for Al alloys observed in the literature varies from 0.01 to 0.08 MPa^{-1}. However, $\alpha = 0.052$ MPa^{-1} has been widely used by many researchers [13, 21, 22]. The value of α can also be defined as $\alpha \approx \beta/n_1$ [15, 30], where β and n_1 are taken as the average values of the slopes of the $\ln(\dot{\varepsilon})$ vs. σ plots and $\ln(\dot{\varepsilon})$ vs. $\ln(\sigma)$ plots, respectively, in the range of T studied. Figure 4 shows the corresponding plots for Alloy-*A*. The values of β and n_1 were evaluated for all the investigated alloys by this procedure. The values of α subsequently determined were 0.016, 0.014, 0.016, 0.013, 0.012, and 0.013 for Alloy-*A* to Alloy-*F*, respectively. α merely facilitates mathematical fitting procedure. Appropriate value of α ensures linear and parallel fits for the $\ln(\dot{\varepsilon})$ vs. $\ln[\sinh(\alpha\sigma)]$ data [13, 20–24, 27, 34, 35]. These plots of $\ln(\dot{\varepsilon})$ vs. $\ln[\sinh(\alpha\sigma)]$ for Alloy-*C* and Alloy-*F* are shown in Figs. 5 and 6, respectively. Considering all the alloys studied, $\alpha = 0.01$ MPa^{-1} yielded the best goodness of fit (R^2) value for the experimental data. Hence in the present analysis, the optimal value of $\alpha = 0.01$ MPa^{-1} was used for all the alloys investigated. In a study of Zr stabilized 2014 Al–Cu–Mg alloy, the calculated Q value remained almost constant for $\alpha \geq 0.04$ MPa^{-1} [21]. For the present investigation, the percentage variation of Q value as calculated for the base alloy, was observed to be quite insignificant ($\leq$5%), for a systematic variation of α from 0.01 to 0.08. In this sense the selection of $\alpha = 0.01$ MPa^{-1} appears to be fully justified for these microalloyed Al–Cu–Mg alloys. It has also been found that the Zener-Hollomon parameter is a useful tool in describing the high temperature deformation behavior of metallic materials.

Zener-Hollomon parameter (Z)

The high temperature flow behavior of materials can be represented by the Zener-Hollomon parameter (Z),

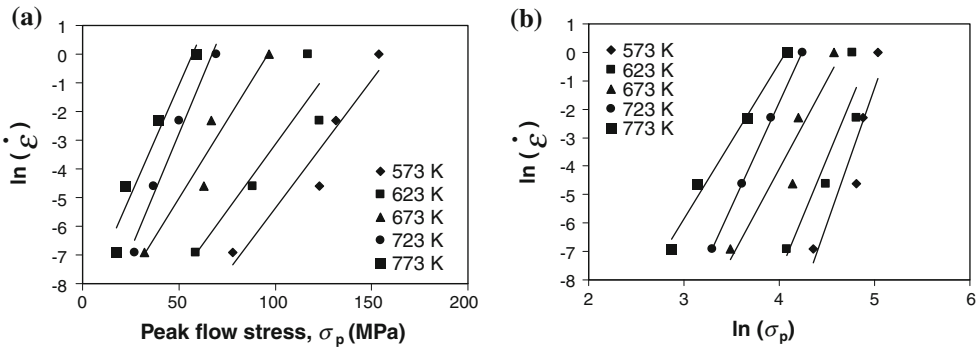

Fig. 4 Plots of **a** $\ln \dot{\varepsilon}$ vs. σ_p and **b** $\ln \dot{\varepsilon}$ vs. $\ln \sigma_p$ for Alloy-*A*

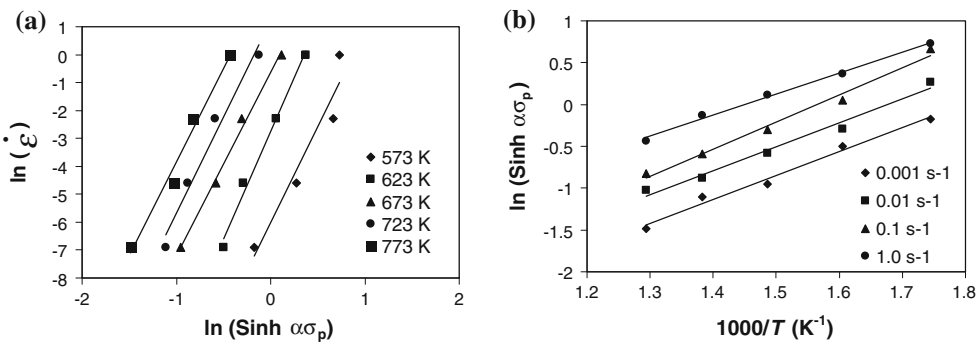

Fig. 5 Plots of **a** $\ln(\sinh \alpha\sigma_p)$ vs. $\ln \dot{\varepsilon}$ and **b** $\ln(\sinh \alpha\sigma_p)$ vs. $1000/T$ for Alloy-*C*

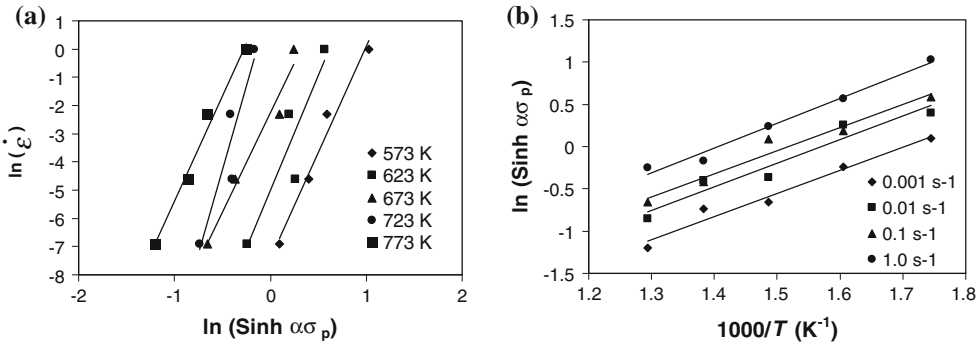

Fig. 6 Plots of **a** ln(sinh $\alpha\sigma_p$) vs. ln $\dot{\varepsilon}$ and **b** ln(sinh $\alpha\sigma_p$) vs. 1000/T for Alloy-F

correlating the strain rate, deformation temperature, and activation energy by the following expression:

$$Z = \dot{\varepsilon}\exp\left(\frac{Q}{RT}\right) \tag{9}$$

Combining Eq. 8 and Eq. 9, the expression for Z can be obtained as:

$$Z = \dot{\varepsilon}\exp\left(\frac{Q}{RT}\right) = A_3[\sinh(\alpha\sigma)]^n \tag{10}$$

Variation of flow stress with deforming conditions can be well illustrated by this Zener-Hollomon parameter (Z) of Eq. 10. This expression can also be written as follows:

$$\ln(Z) = \ln(A_3) + n\ln[\sinh(\alpha\sigma)] \tag{11}$$

where A_3 and n can be determined from the ln(Z) vs. ln[sinh($\alpha\sigma$)] plots [23, 27, 29, 33, 35]. Figure 7 shows the ln(Z) vs. ln[sinh($\alpha\sigma$)] plots of the two selected alloys of Alloy-C and Alloy-F, indicating a fairly good linear fit for the experimental data. The values of ln(Z) for various strain rates and processing temperatures are presented in Tables 3 and 4 for these two alloys. It is evident that Z increases with increase in strain rate and decrease in the deformation temperature, which is similar to the variation of the peak flow stress (σ_p) as revealed from Figs. 1, 2, and 3. Reported literature indicates that DRX is generally favored at low Z values, which correspond to low strain rates and high processing temperatures [24].

Activation energy for deformation

The activation energy (Q) for high temperature deformation can be obtained from a plot of ln($\dot{\varepsilon}$) vs. 1/T at constant [sinh($\alpha\sigma$)] values [26]. The expression for Q therefore becomes:

$$Q = -R\left[\frac{\partial \ln \dot{\varepsilon}}{\partial \frac{1}{T}}\right]_{\sinh(\alpha\sigma)} \tag{12}$$

Equation 12 can also be expressed by the following relationship, which is considered as the general equation for evaluating the activation energy term when the hyperbolic-sine constitutive modeling is being used [15, 20–23, 30, 34, 35]:

$$Q = R\left[\frac{\partial \ln \dot{\varepsilon}}{\partial \ln[\sinh(\alpha\sigma)]}\right]_T \left[\frac{\partial \ln[\sinh(\alpha\sigma)]}{\partial\left(\frac{1}{T}\right)}\right]_{\dot{\varepsilon}}, \quad \text{i.e., } Q = RnS \tag{13}$$

where n is the mean slope of ln($\dot{\varepsilon}$) vs. ln[sinh($\alpha\sigma$)] plots at different T and S is the mean slope of the ln[sinh($\alpha\sigma$)] vs. 1/T plots at various $\dot{\varepsilon}$. These plots for the two selected alloys of Alloy-C and Alloy-F are shown in Figs. 5 and 6, respectively. Table 5 presents the values of n, S, A_3, and Q corresponding to all the Al–Cu–Mg alloys investigated. Figure 8 plots the variation of Q with Sn content in the investigated Al–Cu–Mg alloy system. The Q value of 183.4 kJ mol^{-1} obtained for Alloy-A (base alloy) is in

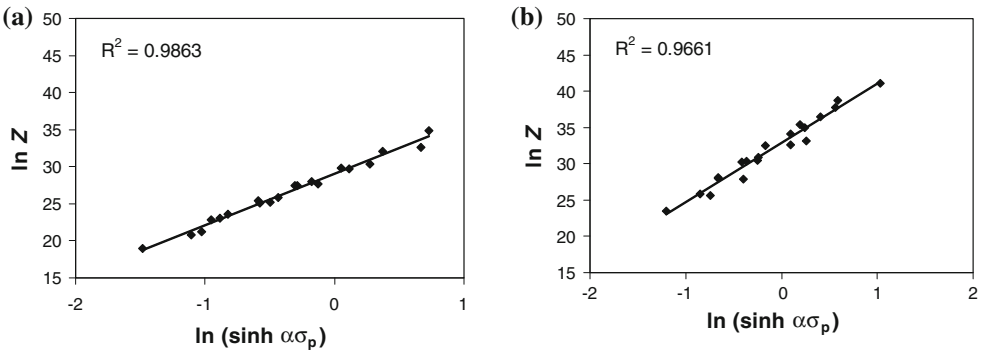

Fig. 7 Plots of ln(sinh $\alpha\sigma_p$) vs. ln Z for **a** Alloy-C and **b** Alloy-F

Table 3 Values of ln(*Z*) for Alloy-*C* at various deformation conditions

$\dot{\varepsilon}$ (s^{-1})	*T* (°C)				
	300	350	400	450	500
0.001	28.01	25.20	22.82	20.76	18.97
0.01	30.31	27.51	25.12	23.06	21.28
0.1	32.61	29.81	27.42	25.37	23.58
1.0	34.91	32.11	29.73	27.67	25.88

Table 4 Values of ln(*Z*) for Alloy-*F* at various deformation conditions

$\dot{\varepsilon}$ (s^{-1})	*T* (°C)				
	300	350	400	450	500
0.001	34.14	30.84	28.04	25.62	23.52
0.01	36.44	33.15	30.34	27.92	25.82
0.1	38.74	35.45	32.64	30.23	28.12
1.0	41.04	37.75	34.95	32.53	30.42

general agreement with the values reported for other Al alloys [13, 20, 22, 29]. However, Q increased to 225.5 kJ mol^{-1} with the addition of 0.08 wt% of Sn while decreased with further Sn additions.

From Table 5 it can be observed that with increase in Sn content from 0 to 0.08 wt%, n increased from 6.24 to 9.09, but decreased with further Sn additions. The A_3 value of the base alloy increased from 7.83×10^{13} to 5.37×10^{16} s^{-1} with trace additions of 0.06 wt% of Sn. Therefore, it could be observed from the present investigation, as revealed from Table 5 that similar to the variation of Q value, all the other material parameters (viz., n and A_3) of the constitutive model increased significantly up to 0.06 or 0.08 wt% of Sn addition.

Prediction of peak flow stress by constitutive analysis

The general expression for the peak flow stress (σ_p) at any deforming condition can be derived from Eq. 8, and the same can be expressed as:

$$\sigma_p = \frac{1}{\alpha}\sinh^{-1}\left[\frac{\dot{\varepsilon}\exp\left(\frac{Q}{RT}\right)}{A_3}\right]^{\frac{1}{n}} \quad (14)$$

The peak flow stresses of the investigated alloys, during deformation at any T and $\dot{\varepsilon}$ combination can thus be determined or predicted from the above mathematical model, since the values of the constant terms of α, n, S, A_3, and Q of Eq. 14 corresponding to all the six investigated alloys are already evaluated as shown in Table 5. To establish confidence of these various constants determined for the presently investigated microalloyed Al–Cu–Mg alloys, the σ_p values corresponding to the T and $\dot{\varepsilon}$ combinations at which experiments were carried out were evaluated using Eq. 14. A comparison of the peak flow stresses determined by Eq. 14 and the experimentally obtained values is given in Tables 6 and 7 for the two selected alloys of Alloy-*C* and Alloy-*F*, respectively. The plots of the predicted versus experimental σ_p values of three selected alloys, Alloy-*A*, Alloy-*C*, and Alloy-*F* are shown in Fig. 9. For perfect prediction, all the points

Table 5 Values of the constants α, n, S, A_3, and Q corresponding to the Al–Cu–Mg alloys

Sample ID	α (MPa^{-1})	n	S	A_3 (s^{-1})	Q (kJ mol^{-1})
Alloy-*A*	0.01	6.24	3.53	7.83×10^{13}	183.4
Alloy-*B*	0.01	6.77	2.86	1.28×10^{12}	161.2
Alloy-*C*	0.01	6.97	2.87	4.16×10^{12}	166.3
Alloy-*D*	0.01	8.55	3.14	5.37×10^{16}	223.3
Alloy-*E*	0.01	9.09	2.98	1.25×10^{16}	225.5
Alloy-*F*	0.01	8.40	2.80	1.96×10^{14}	195.5

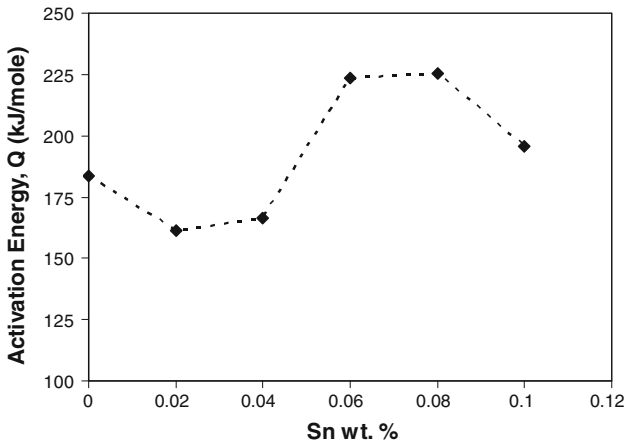

Fig. 8 Variation of activation energy of deformation with Sn content in Al–Cu–Mg alloys

should lie on the solid line inclined at 45° to the *x*-axis. Sets of dashed lines representing the boundaries of ±13% deviations are also shown in the respective figures. The figures show that most of the points lie very close to the line of prefect prediction for the alloys.

It is seen that the percentage error in prediction of σ_p for Alloy-*A* is less than ±13% for 16 out of 20 data values. Although the maximum absolute error in the prediction is −22.6 MPa, the percentage error is only 14.69 for this case. The absolute error is high since the actual stress value is also high. Similarly, for low values of actual stress (viz., 23.15 MPa), though the absolute error is only 4 MPa, the % error shows a high value of 17.27. Errors of these levels are expected when the values which are to be predicted vary over a wide range (e.g., in the present case σ_p varies from 18 to 154 MPa). The percentage error in the prediction of σ_p for Alloy-*D* is less than ±13% for all of 20 data values. Maximum absolute error in the prediction is −10.15 MPa, where the percentage error is 5.96. The RMS errors during σ_p prediction are 8.53, 9.33, 4.84, 3.24, 10.03, and 7.52 for alloys *A*–*F*, respectively. It was also observed that 16, 15, 20, 20, 18, and 17 numbers out of 20 data points (i.e. 80, 75, 100, 100, 90, and 85% of the date sets) fall within ±13% deviation line for the six investigated alloys from Alloy-*A* to Alloy-*F*, respectively. This establishes the confidence in the values of various parameters obtained for prediction of peak flow stress by the constitutive analysis, during high temperature deformation of these microalloyed Al–Cu–Mg alloys.

Microstructural analysis

As already discussed in "Flow stress behavior" section, for most of the combinations of $\dot{\varepsilon}$and *T*, the σ_p value of the investigated Al–Cu–Mg alloy system did not vary significantly with increase in Sn content from 0 to 0.04 wt%. However, with further increase in Sn content up to 0.08 wt%, σ_p value increased abruptly for nearly all $\dot{\varepsilon}$ and *T* combinations. This trend in σ_p is further supported by the

Table 6 Comparison of experimental and predicted values of peak flow stress, σ_p for Alloy-*C*

Strain rate (s^{-1})	Temperature (°C)	Experimental peak flow stress (MPa)	Predicted peak flow stress (MPa)	Error (MPa)	% error
0.001	300	76.35	77.89	−1.54	−2.02
0.001	350	57.67	54.76	2.91	5.04
0.001	400	37.65	39.81	−2.16	−5.73
0.001	450	32.45	29.98	2.47	7.61
0.001	500	22.53	23.33	−0.80	−3.54
0.01	300	108.65	101.39	7.26	6.68
0.01	350	69.24	73.32	−4.08	−5.89
0.01	400	53.51	54.17	−0.66	−1.24
0.01	450	40.29	41.17	−0.88	−2.18
0.01	500	35.10	32.19	2.91	8.28
0.1	300	141.88	128.30	13.58	9.57
0.1	350	122.03	120.50	1.53	1.25
0.1	400	68.39	72.57	−4.18	−6.12
0.1	450	53.10	55.95	−2.85	−5.36
0.1	500	42.66	44.13	−1.47	−3.44
1.0	300	147.79	157.69	−9.90	−6.70
1.0	350	116.65	122.22	−5.57	−4.77
1.0	400	96.38	95.09	1.29	1.34
1.0	450	79.38	74.80	4.58	5.78
1.0	500	60.89	59.78	1.11	1.82

Table 7 Comparison of experimental and predicted values of peak flow stress, σ_p for Alloy-*F*

Strain rate (s^{-1})	Temperature (°C)	Experimental peak flow stress (MPa)	Predicted peak flow stress (MPa)	Error (MPa)	% Error
0.001	300	94.98	98.84	−3.86	−4.07
0.001	350	72.22	71.84	0.38	0.52
0.001	400	49.70	53.41	−3.71	−7.47
0.001	450	46.03	40.84	5.19	11.27
0.001	500	29.62	32.13	−2.51	−8.46
0.01	300	119.29	120.72	−1.43	−1.20
0.01	350	107.41	90.14	17.27	16.08
0.01	400	64.68	68.23	−3.55	−5.49
0.01	450	62.78	52.75	10.03	15.97
0.01	500	41.49	41.77	−0.28	−0.67
0.1	300	135.11	144.49	−9.38	−6.94
0.1	350	102.2	120.50	−18.30	−17.91
0.1	400	94.77	85.92	8.85	9.34
0.1	450	62.00	67.43	−5.43	−8.76
0.1	500	49.62	53.90	−4.28	−8.63
1.0	300	175.22	169.61	5.61	3.20
1.0	350	133.15	134.06	−0.91	−0.68
1.0	400	106.02	106.28	−0.26	−0.24
1.0	450	76.80	84.97	−8.17	−10.64
1.0	500	71.58	68.83	2.75	3.84

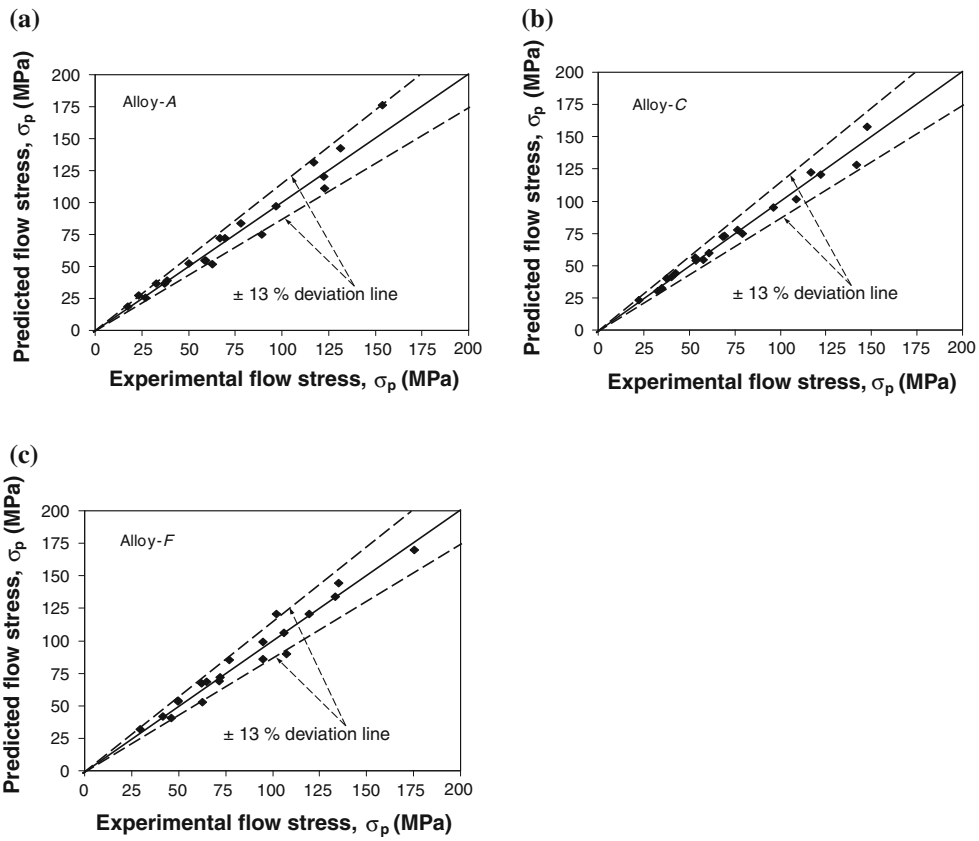

Fig. 9 Variation of predicted σ_p with experimental σ_p for **a** Alloy-*A*, **b** Alloy-*C*, and **c** Alloy-*F*

variation of activation energy (Q), with Sn content, as revealed in Fig. 8. The Q value which actually represents the degree of hindrance to deformation is maximum for the alloys with 0.06 and 0.08 wt% of Sn additions. The peak flow stresses required to deform these two alloys have therefore been observed to be higher compared to the other investigated alloys. In a separate study, when the hardness and tensile properties of these homogenized (same processing condition like that of the hot compression test samples, as mentioned in "Experimental procedures" section) alloys were investigated at room temperature, the Vickers Hardness Number (VHN), yield strength (YS), and ultimate tensile strength (UTS) were observed to hold the similar trend with variation in Sn content. Figure 10 shows the variation in hardness, strength and percentage elongation with Sn content of this Al–Cu–Mg alloy system. Hardness, YS, and UTS of the alloy increased with increase in Sn content up to 0.06 wt%. However, this was achieved at the expense of ductility. Hardness, YS, and UTS gradually decreased upon further additions of Sn. The alloy with 0.06 wt% Sn was observed to have the maximum YS of 99 MPa and UTS of 187 MPa among all the investigated alloys. The YS and UTS of the base alloy increased by 21 and 56%, respectively, whereas the ductility reduced by 9%, upon addition of 0.06 wt% of Sn. It may also be noted that the alloys with Sn exhibited higher strength in comparison to the alloy without Sn. Similar behavior has been reported for the Al–7%Si–0.35%Mg alloy, which acquired the best mechanical properties upon 0.05 wt% of Sn addition [36]. But addition of 0.15 wt% Sn is reported to lower the YS, UTS, and hardness values, and raise the ductility and toughness of these cast alloys. Similar trend of YS and UTS observed in the presently investigated alloy have also been reported for powder metallurgy processed Al–4.4Cu–0.8Si–0.5 Mg alloy with Sn concentration up to 0.1 wt% [8]. The strength values attained a maximum with 0.05 wt% Sn addition, but decreased with further addition of Sn. The percentage elongation of the Al–Cu–Si–Mg alloy was higher due to addition of 0.1 wt% Sn. Following the above-reported trends, 0.1 wt% Sn addition resulted in an increase in ductility in the present Al–Cu–Mg alloy system. Such beneficial increase in strengthening effect with increase in alloying element often gets limited to certain percentage of the alloying element and is apparently a general feature of Al alloys as pointed out by the literature. Strength of the Al–Mg alloy, for example, increased with increase in Sc content up to 0.4 wt%, but decreased with further additions of Sc [37].

However, to justify the above variations in strength as well as σ_p during hot deformation of the presently investigated alloys, it requires a microstructural investigation about the effect of Sn content on these Al–Cu–Mg alloys. It is worthy to mention that these variations in σ_p during hot deformation can not really be attributed to the variation in grain size among the alloys due to trace additions of Sn. The variation of average grain size of the homogenized alloy with Sn content is plotted in Fig. 11. The figure shows a marginal increase in the average grain diameter from 16 to 19 μm as the Sn content is increased from 0 to

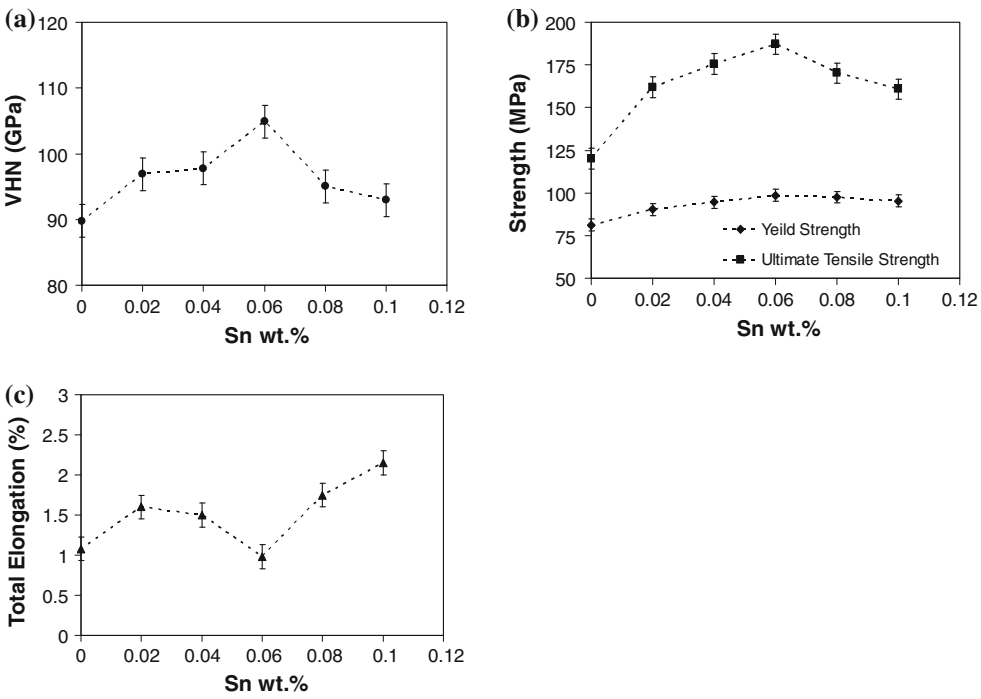

Fig. 10 Variation of **a** Vickers Hardness Number (VHN), **b** strength, and **c** ductility of homogenized Al–Cu–Mg alloys as a function of Sn wt%

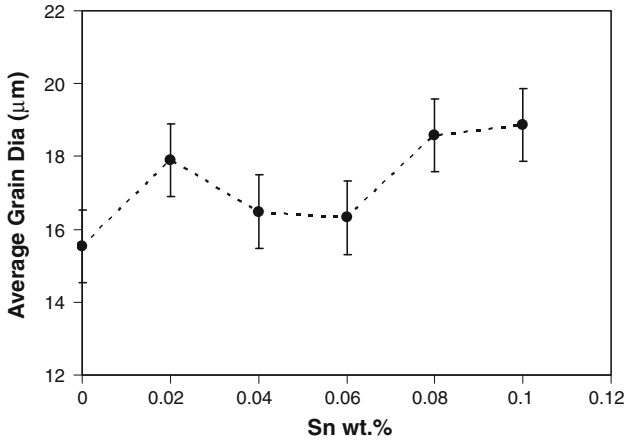

Fig. 11 Variation of average grain size with Sn content of cast and homogenized Al–Cu–Mg alloys

0.1 wt%. This shows that microalloying the base alloy with Sn has no significant influence on the grain refinement during casting.

However, the variation in strength and σ_p value may be correlated with the second phases evolved at the grain boundaries, with trace additions of Sn. Figure 12a–c shows the SEM micrographs of the homogenized (same processing condition like that of the hot compression test samples, as mentioned in "Experimental procedures" section) Al–Cu–Mg alloys containing 0, 0.06, and 0.1 wt% of Sn, respectively. SEM micrographs of the homogenized samples revealed two different types of phases present at the grain boundary regions: a white platelet-like phase (Phase-*C*) and a gray discontinuous platelet-like phase (Phase-*D*). With increase in Sn content up to 0.06 wt%, the volume of Phase-*D* increased and at the same time the morphology of this phase changed from a discontinuous platelet form to script form. On further increase in Sn wt%, it was observed that the Phase-*D* did not show script-like features. Maximum amount of Phase-*D* was observed for the Alloy-*D* with 0.06 wt% of Sn content. EDS analysis of the two phases present in the matrix of the homogenized alloys are given in Table 8. The matrix composition in all cases was found to be $Al_{99.3}Cu_{0.5}Mn_{0.2}$. Phase-*C* was identified to be θ-phase ($CuAl_2$) and its volume fraction and morphology remained unchanged with subsequent Sn additions. However, the composition of Phase-*D* varied with trace additions of Sn. The amount of Mn present in Phase-*D* decreased upon subsequent Sn additions in the

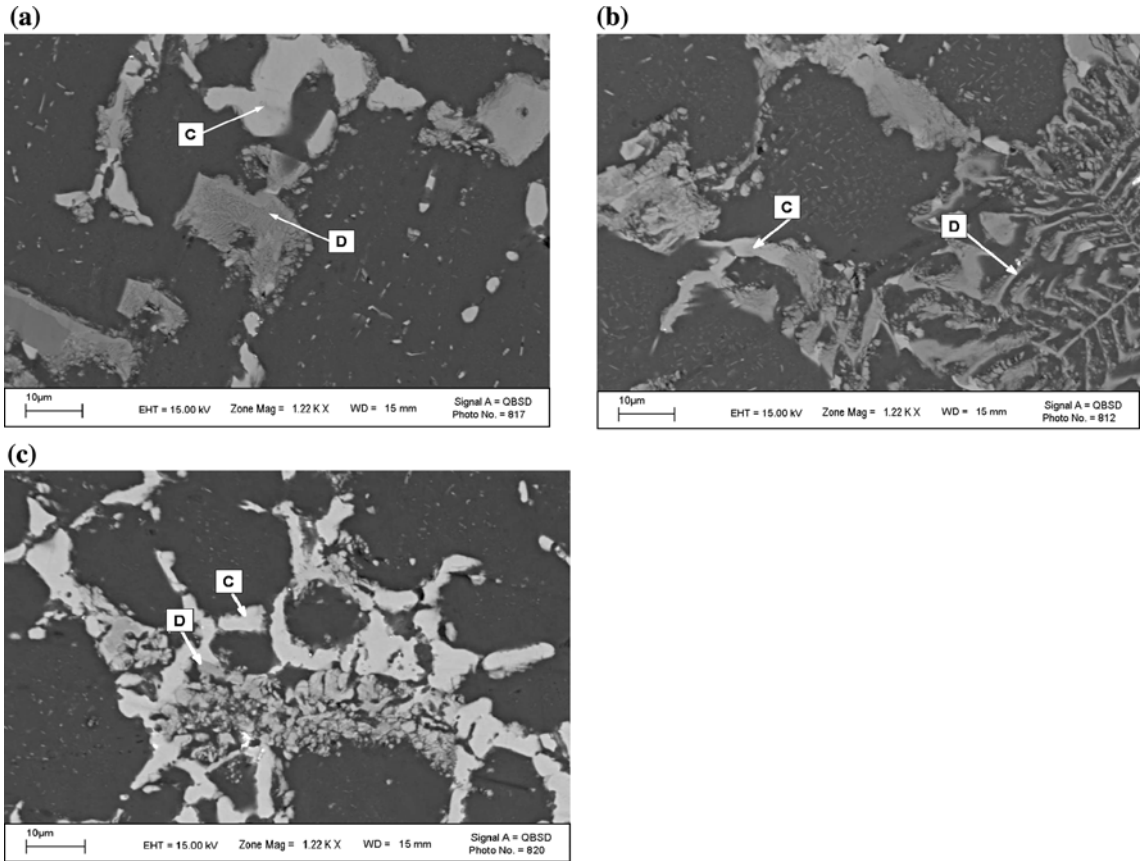

Fig. 12 SEM micrographs of homogenized **a** Alloy-*A*, **b** Alloy-*D*, and **c** Alloy-*F* showing the grain boundary phases

Table 8 Compositions of different phases in the homogenized alloys

Alloy designation	Matrix	Phase-*C*	Phase-*D*
Alloy-*A*	$Al_{99.3}Cu_{0.5}Mn_{0.2}$	$CuAl_2$	$Al_{75.9}Cu_{1.3}Si_{5.9}Fe_{8.3}Mn_{8.6}$
Alloy-*B*	$Al_{99.3}Cu_{0.5}Mn_{0.2}$	$CuAl_2$	$Al_{78.5}Cu_{3.6}Si_{5.6}Fe_{7.9}Mn_{4.4}$
Alloy-*C*	$Al_{99.3}Cu_{0.5}Mn_{0.2}$	$CuAl_2$	$Al_{79.5}Cu_{4.1}Si_{5.4}Fe_{7.3}Mn_{3.7}$
Alloy-*D*	$Al_{99.3}Cu_{0.5}Mn_{0.2}$	$CuAl_2$	$Al_{78.9}Cu_{4.5}Si_{6.2}Fe_{7.0}Mn_{3.4}$
Alloy-*E*	$Al_{99.3}Cu_{0.5}Mn_{0.2}$	$CuAl_2$	$Al_{77.9}Cu_{5.3}Si_{6.4}Fe_{7.5}Mn_{2.9}$
Alloy-*F*	$Al_{99.3}Cu_{0.5}Mn_{0.2}$	$CuAl_2$	$Al_{70.9}Cu_{9.8}Si_{6.2}Fe_{11.0}Mn_{2.1}$

homogenized alloys. The Phase-*D* observed in the alloys is similar to the previously reported plate-like Fe–Mn–Cu–Si–Al phase observed in some aluminum alloys [12, 38]. The higher strength (with lower ductility) of Alloy-*D* at room temperature as well as higher value of σ_p (during hot deformation) of the investigated Al–Cu–Mg alloys with 0.06 and 0.08 wt% of Sn contents can be attributed to the variation in amount, composition and morphology of the Phase-*D*. The morphology of the Phase-*D* changed from platelet form to script form and the amount of this phase increased with increase in Sn content up to 0.06 wt%. The Cu content in Phase-*D* increased with increase in Sn wt% with a concomitant decrease in Mn. It appears that the failure of the material may have initiated at regions containing a preponderance of Phase-*D*. However, in spite of the higher strength values obtained for Alloy-*D* and Alloy-*E*, these alloys are relatively difficult to deform as revealed from the higher value of peak flow stress, as well as the high activation energy for hot deformation.

As already discussed in "Zener-Hollomon parameter (*Z*)" section, DRX is generally favored at low *Z* values, which correspond to low strain rates and high processing temperatures [24]. DRX in Al alloys has been observed to occur at lower $\dot{\varepsilon}$ and is sensitive to the impurity content [39]. The flow softening with increase in ε, as clearly revealed from some of the flow curves of Figs. 1, 2, and 3, is a direct consequence of this DRX phenomenon. To study the dissipative microstructures formed during hot deformation, the microstructures of specimens deformed to a ε of 0.6 under various $\dot{\varepsilon}$ and *T* were observed using OM. The microstructures of Alloy-*A*, Alloy-*D*, and Alloy-*F*, deformed at $T = 500$ °C and $\dot{\varepsilon} = 0.001\ s^{-1}$, as shown in Fig. 13, reveal small recrystallized grains at the grain boundaries, which indicate partial recrystallization or the initiation of the recrystallization process. The grain boundaries are irregular in shape. Nucleation of these fine crystals in the matrix during hot deformation, especially at the grain boundary regions is the typical feature of DRX. DRX is a beneficial process [40] in hot deformation since it not only gives a stable flow and good workability to the material by simultaneously softening it, but also

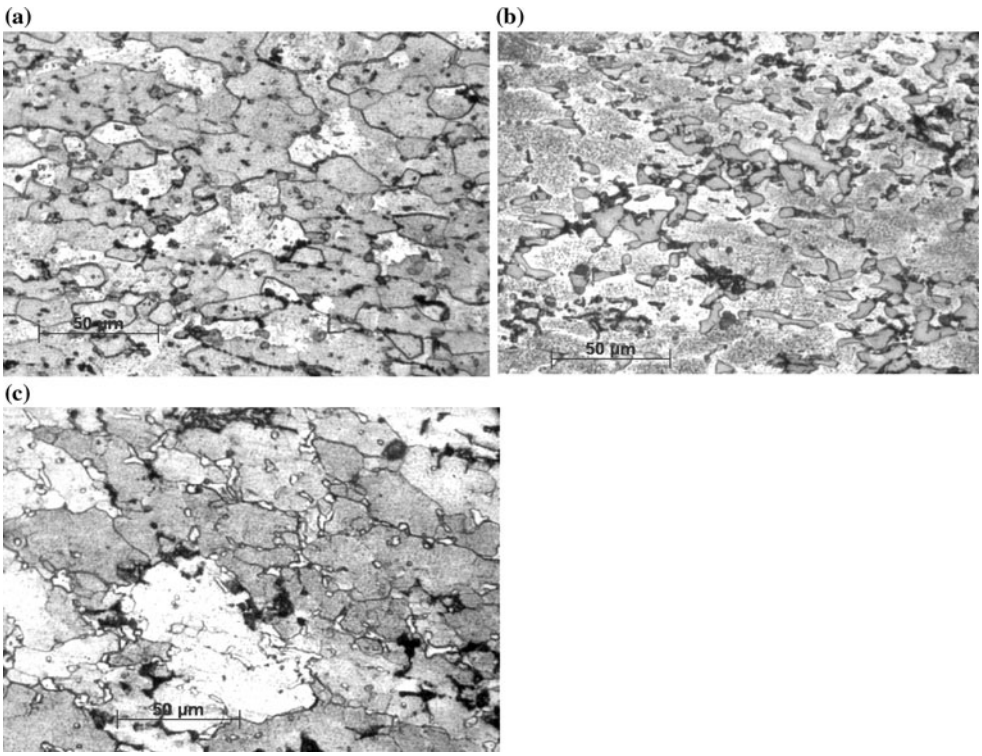

Fig. 13 Optical micrographs showing DRX in **a** Alloy-*A*, **b** Alloy-*D*, and **c** Alloy-*F* deformed at $\dot{\varepsilon} = 0.001\ s^{-1}$, $T = 500$ °C

reconstitutes the microstructure [41]. The presently investigated material can therefore be deformed safely with ease, at very low strain rates and high deformation temperatures.

Precipitation strengthening and activation energy for precipitation

The variations in σ_p value and activation energy (Q) for hot deformation may well be attributed to the influence of trace additions of Sn on the second phase precipitation reactions and the subsequent activation energy of precipitation. DSC studies were undertaken to understand the kinetics of the precipitation reaction of the investigated alloys. The kinetic parameters of the rate equation were determined from the experimental results. The rate equations relating rate of transformation, molar fraction of precipitates, temperature and activation energy were arrived for all the alloys. The activation energy (ΔE) for the reaction peaks and the effect of Sn addition on ΔE were determined. XRD studies were resorted to identify possible precipitation or crystallization occurring at the temperature ranges revealed from the DSC thermograms.

Calorimetry has been employed since 1930s to study precipitation reaction(s) in Al–Cu alloys [42–46]. These studies cite the observation of several peaks in the thermograms, which have been assigned to specific reactions. These reports show that in spite of a general agreement, the features observed vary depending upon the processing conditions of the alloys. In one such study, 2219 Al alloys were processed under different thermo-mechanical conditions such as T31, T42, T81, T87, T851, and O tempers [47]. Interestingly, the DSC curves showed four features for the alloys processed under T31 and T42 tempers, viz., an endothermic (dissolution) reaction between 50 and 200 °C, an exothermic (precipitation) reaction between 200 and 300 °C, multiple endothermic (dissolution) reactions between 300 and 550 °C, and a superimposed exothermic (precipitation) reaction between 400 and 475 °C. DSC curves of samples aged at elevated temperatures do not show many of these reactions. These studies have established that the positions and the number of features observed in the DSC curves of Al–Cu–Mg alloys depend strongly on the composition and processing conditions. The exothermic reaction occurring between 200 and 300 °C and the melting endotherm around 500 °C appear to be the common features observed in all conditions in these alloys. It is now well established that the exothermic reaction occurring between 200 and 300 °C is the signature of precipitation of θ' [47].

In the current investigations, DSC curves of the alloys were obtained at constant heating rates (ϕ) of 10, 15, 20, and 25 °C min^{-1}. The DSC was set to record exothermic reactions as downward heat flow peaks (troughs) and vice versa. The area under the peak gives the value of enthalpy of the respective reaction. The DSC curves of all the samples exhibited two features, viz., one in the temperature range of 200 to 300 °C and the other in the temperature range of 450 to 550 °C. The exothermic peak(s) in the low temperature range correspond to the precipitation reaction(s), whereas the endotherm(s) at the high temperature range correspond to the melting of the alloy phase(s). Figure 14 shows the truncated parts of the DSC curves obtained at different heating rates in the temperature range of 200 to 350 °C where the precipitation reaction(s) was (were) observed for the base alloy (Alloy-*A*), and the one microalloyed with 0.06 wt% of Sn (Alloy-*D*). The figure clearly indicates two exothermic (θ' precipitation reaction) peaks in the DSC curves obtained in the heating cycle of these two alloys. For Alloy-*A,* the first peak was observed in the temperature range from 245 to 258 °C and the second peak in the temperature range from 267 to 288 °C. The corresponding temperature ranges were 233 to 252 °C and 271 to 297 °C, respectively, for Alloy-*D*. For all the other alloys, only one broad exothermic peak could be observed in the temperature range from 250 to 300 °C. Grain boundaries are regions of higher energy than the regions well inside the grains. Due to this reason, early nucleation of the precipitate phase occurs at the grain boundaries. The DSC curves of Alloy-*A* and Alloy-*D* revealed that the

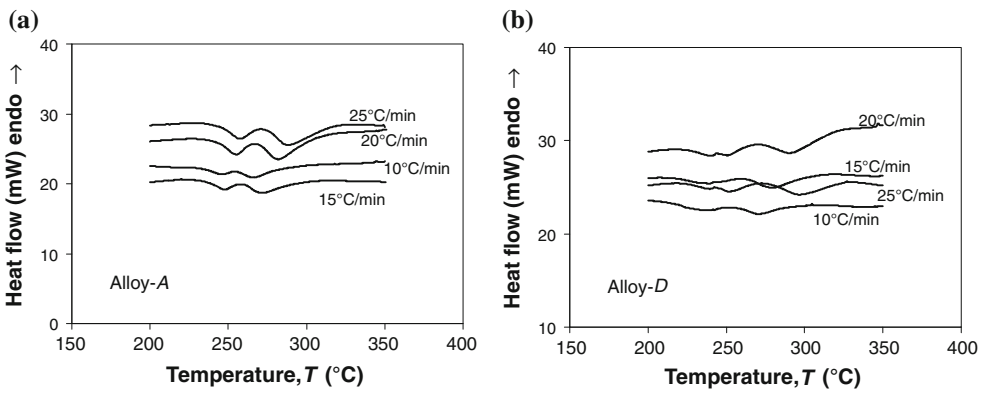

Fig. 14 DSC curves highlighting the exothermic peaks observed at different heating rates for **a** Alloy-*A* and **b** Alloy-*D*

precipitation reaction occurs in two stages, which shows that precipitation at the grain boundaries precedes the precipitation inside the grains. The two well-resolved exothermic peaks in the DSC curves of Alloy-*A* indicate two-step precipitation mechanism. Upon microalloying with Sn, the nature of these precipitation reactions varied indicating that Sn present in the grain boundaries and inside the grains influences the respective precipitation mechanisms. It has to be pointed out that it is difficult to distinguish if the two exotherms were overlapping especially when the reaction enthalpy is low. Hence the present reasoning is based on the DSC data obtained for the investigated alloys. The onset (T_o), peak (T_p), and end (T_e) temperatures of both the exothermic peaks were determined from the DSC curves. The peak temperature (T_P) of both exothermic peaks increased with increase in heating rate for all the alloys. This behavior is expected in any kinetically driven reaction, hence the reaction kinetics can be interpreted using kinetic relations.

The mole fraction $Y(T)$ transformed at any temperature T, can be determined by evaluating the partial area under the reaction curve by:

$$Y(T) = \frac{A(T)}{A(T_e)} \tag{15}$$

where $A(T)$ is the area under the corresponding peak between onset temperature (T_o) and a given temperature T and $A(T_e)$ is the total area under the peak from T_o to peak end temperature (T_e). The shift in the peak temperatures with change in heating rate indicates that the reaction is kinetically controlled and the rate of reaction is generally expressed as [48]:

$$\frac{\partial Y}{\partial t} = f(Y) k_0 e^{-\frac{\Delta E}{RT}} \tag{16}$$

where $f(Y)$ is a function of mole fraction transformed Y, k_0 is the frequency factor, ΔE is the activation energy for the reaction, and R is the universal gas constant.

Expressing the rate of transformation with respect to time, Eq. 16 can be rewritten in terms of temperature, since ϕ is the constant heating rate $\left(\phi = \frac{\partial T}{\partial t}\right)$:

$$\frac{\partial Y}{\partial T}\phi = f(Y) k_0 e^{-\frac{\Delta E}{RT}} \tag{17}$$

Taking logarithm on both sides, Eq. 17 can be expressed as:

$$\ln\left[\left(\frac{\partial Y}{\partial T}\right)\phi\right] = \ln[f(Y)\, k_0] - \frac{\Delta E}{R}\left(\frac{1}{T}\right) \tag{18}$$

The activation energy (ΔE) for the reaction is determined from the mean slope of plots of $\ln[(dY/dT)\phi]$ vs. $(1000/T)$ for given Y values, where the function $f(Y)$ is not required to be known. In the present study, the same plots are made for a wide range of Y values from 0.1 to 0.9, so as to obtain a good estimation of the ΔE values for the reaction peaks of the alloys. Figure 15a shows the plots of $\ln[(dY/dT)\phi]$ vs. $(1000/T)$ for selected Y values of 0.2, 0.5, and 0.9, for the first exothermic peak of Alloy-*A*. The ΔE values were obtained for different mole fractions and the mean activation energy evaluated for this reaction peak is 105.4 kJ mol^{-1}. Similarly, these plots are shown in Fig. 15b for the second exothermic peak of Alloy-*A*. Mean ΔE value was determined as 78.0 kJ mol^{-1}. The activation energy values for the precipitation peaks were evaluated for all the investigated alloys.

Figure 16 shows the variation in ΔE value with Sn wt% for the first exothermic peak in the DSC curves of the investigated Al–Cu–Mg alloys. ΔE value was observed to gradually decrease with Sn content up to 0.06 wt% and then rapidly increase with further additions of Sn. This observation shows that addition of Sn up to 0.06 wt% enhances the precipitation reaction as depicted by the gradually decreasing ΔE value. However, further addition of Sn does not favor the precipitation process as indicated by a steep increase in ΔE. ΔE value for the second exothermic reaction was 78.0 kJ mol^{-1} for the base alloy (Alloy-*A*) whereas it was found to be 69.0 kJ mol^{-1} for the alloy with 0.06 wt% Sn (Alloy-*D*). The lower value of ΔE of the second exothermic peak obtained for the alloy with 0.06 wt% Sn shows that Sn addition favors the second precipitation reaction. The increasing trend of σ_p value and activation energy (Q) for hot deformation up to 0.06 wt%

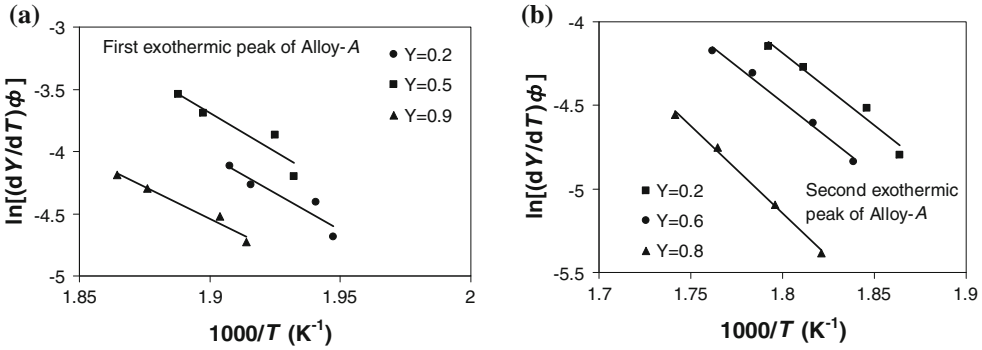

Fig. 15 Plots of $\ln[(dY/dT)\phi]$ vs. $(1000/T)$ for given Y values corresponding to the **a** first exothermic peak and **b** second exothermic peak of Alloy-*A*

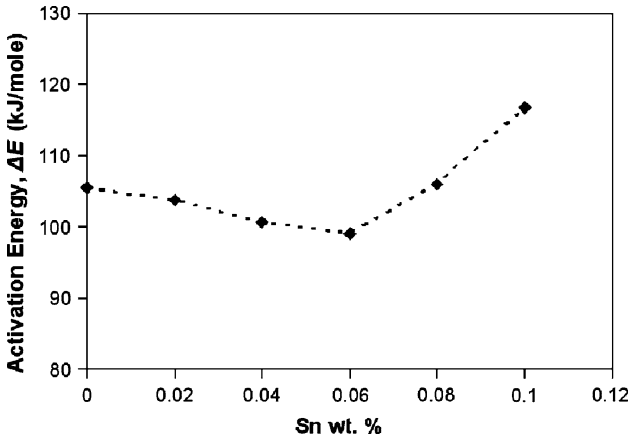

Fig. 16 Variation of activation energy of the first exothermic peaks with Sn content of the Al–Cu–Mg alloys

of Sn addition, and a decrease in the same values with further Sn additions may thus be attributed to the variation in ΔE value of precipitation reactions. When the ΔE value of the precipitation process is low, as depicted in the case of Alloy-*D* (with 0.06 wt% of Sn), the precipitation reaction is favored. At this level of Sn content, the precipitation kinetics is accelerated, enhancing the heterogeneous precipitation sites and helping in nucleation and growth of the metastable θ' phase. The dispersed precipitates retard the dislocation slips, which subsequently enhance the strength, σ_p value and the activation energy (Q) for plastic deformation. In Al–Cu alloy system, the final stable precipitate is generally $CuAl_2$ (θ), which is formed through a number of intermediate stages, viz., GP1 zones → GP2 zone θ'' (thin discs, fully coherent with the matrix) → θ' (disc shaped and semi-coherent with the matrix → θ ($CuAl_2$, which is spherical and incoherent at the precipitate–matrix interface).

XRD studies were performed to identify the crystalline phase(s) formed during the precipitation reaction. The peak reaction temperatures were already determined using DSC technique. In order to identify the crystalline phases precipitating at these temperatures, three selected alloys (Alloy-*A*, Alloy-*D*, and Alloy-*F*) were first solutionized at 500 °C followed by water quenching. After the solutionizing heat treatment, the samples were aged at 350 °C for 10 h (just after the completion of the precipitation reactions) and water quenched. Figure 17 shows the XRD patterns of the three selected alloys in aged and water quenched condition.

Analysis of the XRD patterns reveals the presence of $CuAl_2$ along with the Al matrix as major phases in all the processed alloys. The Al matrix phase has been identified as a face centered cubic crystal with space group *Fm3m* and lattice parameter $a = 4.049$ Å. The $CuAl_2$ phase exhibited tetragonal crystal structure with *I4/mcm* space group and lattice parameters, $a = 6.053$ Å and $c = 4.870$ Å. These structural data are in agreement with those reported in the literature [49–51]. Trace amounts of Sn in Alloy-*D* and Alloy-*F* did not show any noticeable influence on the unit cell volume of the two constituent phases.

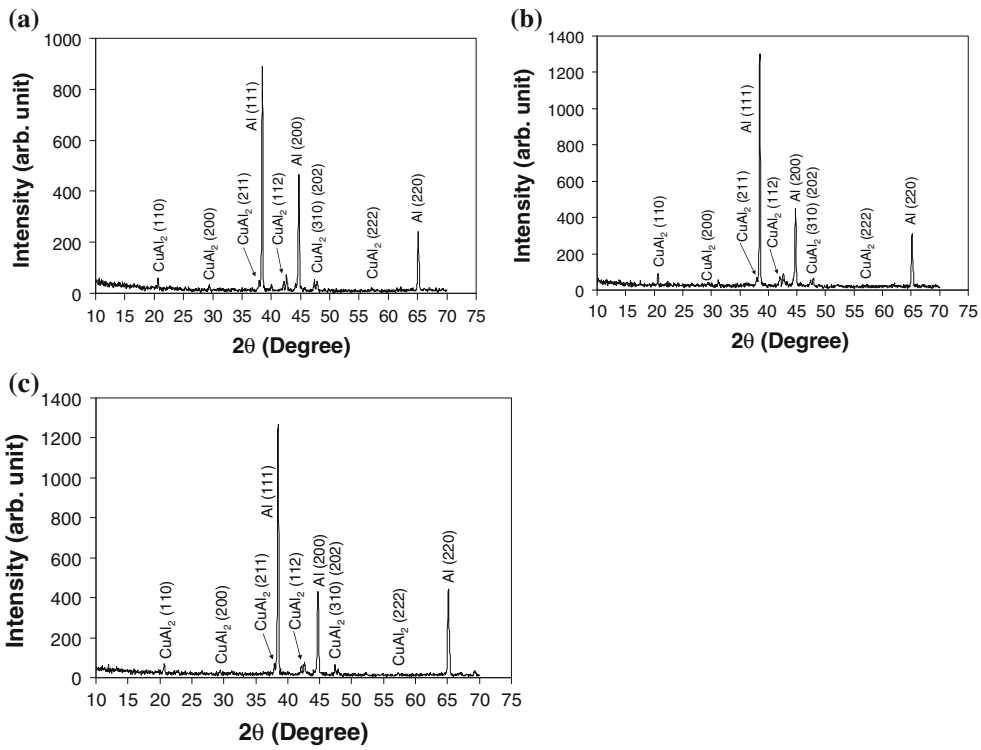

Fig. 17 XRD patterns of aged and water quenched **a** Alloy-*A*, **b** Alloy-*D*, and **c** Alloy-*F*

Several investigations have been carried out on the influence of adding trace amounts (<0.1 wt%) of different alloying elements on the microstructure and mechanical properties of some commercial aluminum alloys. Even small variations in compositions and microstructure have been found to result in major changes in strength, toughness, ductility, and other properties of the alloy. Therefore, microalloying with different elements like Sn, Cd, In, Ag, Si, etc., is being exploited to develop materials with improved properties. Microalloying is generally attempted in precipitation hardenable Al alloys mainly because of the fact that high strength Al alloys are invariably precipitation hardenable alloys. It is to be noted that the influence of trace content of Sn on the Al–Cu–Mg alloys has not been extensively explored.

Monte Carlo computer simulation was carried out to understand the role of the microalloying elements in several Al alloys such as Al–Cu, Al–Li–Cu, and Al–Cu–Mg [7]. Pair interactions between same atomic species, between different atomic species and between an atom and a vacancy were obtained from these studies. Small addition of Mg to Al–Cu alloys exhibited strong tendency to form Mg/Cu/vacancy complexes. Combined addition of Ag or Si with Mg significantly increased the number of Mg/Cu/vacancy complexes in Al–Cu–Mg alloys. From the comparison with experimental results, these complexes are regarded as effective heterogeneous nucleation sites for GP zones, GPB zones (Guinier–Preston–Bagaryatsky zones, which are rod-shaped precipitating particles in Al–Cu–Mg alloys) and/or the Ω phase. Through this work, it was possible to analyze the role of some of the microalloying elements in terms of their characteristic features and applicability.

Liu et al. [51] reported accelerated age hardening and increase in the peak hardness with better thermal stability for Al–Cu–Mg–Mn–Zr alloy containing 0.48 wt% of Ag. However, no effect on grain refinement or recrystallization was observed in this case. The yield strength was found to increase with increase in Ag content at both room and elevated temperatures with concomitant reduction in ductility. Moreover, the strength observed by the addition of Ag is higher than that due to θ' precipitation. This is attributed to the formation of fine plate-like Ω precipitates in Al {111} planes. The effect of Ag on age hardening and mechanical properties was further substantiated by studies on 2519 Al alloys [52, 53]. Brittle modes of fracture reduced the ductility in these alloys upon Ag addition. Addition of 0.3 wt% Ag in 2519 Al alloy accelerated age hardening and increased peak hardness at a precipitation temperature of 180 °C. The effect of 0.2–0.51 wt% Si and 0.69 wt% Ge additions on the microstructure and hardness of 2219 aluminum alloy during aging was investigated by Maksimovic et al. [12]. It was found that for the same level of microalloying, the alloy 2219SG (containing Si and Ge) achieved a maximum hardness three times faster than in alloy 2219S (without Ge). The precipitation kinetics was accelerated due to the presence of fine Si–Ge particles which act as heterogeneous precipitation sites for the metastable θ" phase. Addition of small amount of Ge also increased the hardness as compared to the alloy 2219S (without Ge).

Spray-deposited Al–5Cu–0.4Mg–0.4Ag–0.4Ti alloys containing trace elements of Zr and Mn exhibiting high strength and fracture toughness have been developed for use at ambient and moderately high temperatures [54]. Better mechanical properties were observed in age hardened alloys. Addition of 0.15 wt% Zr and 0.2 wt% Mn exhibited a combination of high fracture toughness and yield strength during aging at temperatures up to 180 °C. The mechanical properties of the alloys were better than those of conventional 2xxx series aluminum alloys. Addition of 0.5 wt% Zr and 0.4 wt% Mn in Al–4Cu–0.8 Mg–0.4Ag alloy resulted in the best combination of yield strength and fracture toughness ever achieved for an aluminum alloy. For example, at 23 °C, the 0.2% offset yield strength ($R_{P0.2}$) and fracture toughness (K_{IC}) values were 378 MPa and 100 MPa $m^{1/2}$, respectively, in the 'T4' temper condition. However, in the 'T6' temper condition the corresponding values were 452 MPa and 77 MPa $m^{1/2}$, respectively. The superior mechanical properties obtained were influenced by the microstructural characteristics, viz., size, density, and distribution of the precipitates as revealed by TEM studies. The microstructure and high temperature stability of age hardenable 2219 aluminum alloy (Al–6.3wt%Cu alloy) modified by 0.2 to 0.8 wt% of Sc, Mg, and Zr additions were investigated by Naga Raju *et al.* [4]. Addition of Sc, Mg, and Zr to the base metal resulted in improved high temperature stability due to formation of fine equiaxed grains, refined eutectics, and large number of high temperature stable and finer precipitates. Out of all the compositions studied by them, the alloy with 0.8% Sc + 0.45% Mg + 0.2% Zr was found to be the best in terms of high temperature stability. Sc addition up to 0.4 wt% increased the strength of Al–Mg alloys [55]. The strengthening was due to the direct hardening by formation of dispersed Al_3Sc particles in the matrix and the substructural hardening for preservation of non-recrystallized structure. Addition of Zr intensified the effect of Sc addition and stabilized the structure of these alloys. Trace addition of Sc was found to improve the yield strength more than the tensile strength of Al–6wt%Mg alloys [37]. This is due to the fine coherent Al_3Sc precipitates being more responsive to the yield behavior. The beneficial strengthening effect of these alloys was, however, found to be limited to 0.4 wt% of Sc addition.

Very few reports are available on the effect of Sn addition on heat treatable aluminum alloys. The reported

results on the effect of trace additions of Cd, In, or Sn on the nucleation and growth of θ' phase in Al–Cu alloys have been compared [10]. Trace additions of Cd, In, and Sn resulted in accelerated aging and higher peak hardness in Al–Cu alloys. This phenomenon was reported to be due to the formation of very small diameter platelets of θ' in alloys containing Sn. The growth rate of θ' platelets in these alloys was found to be very slow. Two mechanisms have been proposed for the θ' formation during precipitation heat treatment of Al–Cu alloys microalloyed with X (where $X = $ Cd, In, or Sn), viz., (i) heterogeneous nucleation on small particles containing trace elements X at temperatures of 200 °C and above and (ii) incorporation of atoms of X into the θ' nuclei resulting in reduced misfit between θ' and the aluminum matrix at lower temperatures. Investigation of trace additions of Sn revealed the precipitation of β-Sn particles within the $CuAl_2$ network and fine Mg_2Sn precipitates in the eutectic Si phase present in Al–Si–Cu–Mg and Al–Si–Mg alloys, respectively [36]. Emadi et al. [56] studied the effect of Sn on the mechanical properties of 319 Al alloys. Although Sn addition did not affect the UTS, it reduced the yield strength and hardness at concentration levels above 0.035% during heat treatment. The elongation was found to increase from 0.7% to more than 1.1%. Investigations on the effect of trace additions of Sn and different heat treatments on the microstructure and mechanical properties of sintered 2xxx series Al–4.4Cu–0.8Si–0.5 Mg alloys have been carried out [8]. Sn concentration was limited to $\leq$0.1 wt% to avoid incipient melting during solution treatment. The study revealed a tensile strength of 375 MPa, which was almost 20% higher than that of the alloy without Sn. Considering these previous reports, the present investigation is an attempt to throw light on the influence of systematic trace additions of tin (Sn) on the high temperature deformation/flow behavior of highly applicable wrought 2xxx series of Al–Cu–Mg alloys, to develop the parameters of the constitutive model for predicting the peak flow stress value and subsequently to vilify the microstructural evolution governing the variation in flow stress of these materials.

Conclusions

(1) The high temperature deformation behavior of Al–5.9wt%Cu–0.5wt%Mg alloys containing $0 \leq$ Sn $\leq$ 0.1 wt% was investigated by hot compression tests performed at temperatures ranging from 300 to 500 °C and strain rates ranging from 0.001 to 1.0 s^{-1}.

(2) Peak flow stress for all the investigated alloys increased with increase in strain rate from 0.001 to 1.0 s^{-1}, and decrease in deformation temperature from 500 to 300 °C.

(3) Flow softening after attaining the peak stress value was observed in all the investigated alloys at low strain rate of 0.001 s^{-1}. Undulations were observed in the flow curves of the alloys microalloyed with Sn at low strain rates and lower deformation temperatures.

(4) No significant variation could be observed in the peak flow stress value of the investigated Al–Cu–Mg alloy system with increase in Sn content from 0 to 0.04 wt%. However, with further increase in Sn content up to 0.08 wt%, peak stress value increased abruptly for all strain rate and temperature combinations.

(5) The activation energy of hot deformation for alloys with Sn wt% >0.04 was higher than that of the base alloy. The high activation energy of the alloys with Sn wt% >0.04 shows that these alloys are relatively difficult to deform, in spite of exhibiting better mechanical properties.

(6) The constitutive constants, α, n, and A_3, were determined from the experimental results for all the investigated alloys. The solved constitutive equations for high temperature deformation yielded good prediction of peak flow stress for all the alloys within the range of temperatures and strain rates investigated, and within a percentage deviation of $\pm$13% with fairly good accuracy. The peak flow stresses during deformation were predicted using the above lay within an RMS error of 8.53, 9.33, 4.84, 3.24, 10.03, and 7.52 for alloys *A*–*F*, respectively.

(7) SEM micrographs revealed two types of second phases at the grain boundary regions of the homogenized alloy matrix. One of them was Al–Cu–Si–Fe–Mn phase having script morphology. The other phase was identified as "θ" phase of $CuAl_2$.

(8) The higher strength as well as high temperature peak flow stress value of the investigated Al–Cu–Mg alloys with 0.06 and 0.08 wt% of Sn contents may be attributed to the variation in amount, composition and morphology of the Al–Cu–Si–Fe–Mn phase present at the grain boundaries.

(9) The flow softening with increase in ε as observed at low strain rates and high processing temperatures for the investigated alloys, is a direct consequence of DRX phenomenon, which reconstitutes the microstructure simultaneous to the hot deformation process.

(10) The trend in σ_p value and activation energy (Q) for hot deformation with Sn addition is influenced by the variation in activation energy (ΔE) of precipitation reaction. The precipitation reaction is favored with 0.06 wt% of Sn content, as depicted by the low ΔE value. The dispersed precipitates retard the dislocation slips, which subsequently enhance the

strength, σ_p value and the activation energy for plastic deformation.

Acknowledgements The authors are thankful to Mr. Rituraj Saikia and Mr. Sanjib Sarma, Department of Mechanical Engineering, Indian Institute of Technology Guwahati, for their useful assistance during conduction of high temperature compression tests.

References

1. Heinz A, Haszler A, Keidel C, Moldenhauer S, Benedictus R, Miller WS (2000) Mater Sci Eng A 80:102
2. ASM International Handbook Committee (1990) ASM handbook, Volume 02 – Properties and selection: nonferrous alloys and special-purpose materials. ASM International
3. Sukumaran K, Ravikumar KK, Pillai SGK, Rajan TPD, Ravi M, Pillai RM, Pai BC (2008) Mater Sci Eng A 490:235
4. Naga Raju P, Srinivasa Rao K, Reddy GM, Kamaraj M, Prasad Rao K (2007) Mater Sci Eng A 464:192
5. Wang J, Yi D, Su X, Yin F (2008) Mater Charact 59:965
6. Yu K, Li W, Li S, Zhao J (2004) Mater Sci Eng A 368:88
7. Hirosawa S, Sato T, Kamio A, Flower HM (2000) Acta Mater 48:1797
8. Sercombe TB, Schaffer GB (1999) Mater Sci Eng A 268:32
9. Schaffer GB, Huo SH, Drennan J, Auchterlonie GJ (2001) Acta Mater 49:2671
10. Silcock JM, Flower HM (2002) Scripta Mater 46:389
11. Ocenasek V, Slamova M (2001) Mater Charact 47:157
12. Maksimovic V, Zec S, Radmilovic V, Jovanovic MT (2003) J Serb Chem Soc 68(11):893
13. McQueen HJ, Ryan ND (2002) Mater Sci Eng A 322:43
14. McQueen HJ, Kassner ME (2005) Mater Sci Eng A 410–411:58
15. Liang WJ, Pan QL, He YB, Li YC, Zhang XG (2008) J Cent South Univ Technol 15:289
16. Cho JR, Bae WB, Hwang WJ, Hartley P (2001) J Mater Process Technol 118:356
17. Smith TJ, Maier HJ, Sehitoglu H, Fleury E, Allison J (1999) Metall Mater Trans A 30A:133
18. Kaibyshev R, Sitdikov O, Mazurina I, Lesuer DR (2002) Mater Sci Eng A 334:104
19. Kaibyshev R, Kazakulov I, Gromov D, Musin F, Lesuer DR, Nieh TG (2001) Scripta Mater 44:2411
20. Cavaliere P (2002) J Light Met 2:247
21. Spigarelli S, Cabibbo M, Evangelista E, Bidulska J (2003) J Mater Sci 38:81. doi:10.1023/A:1021161715742
22. Bardi F, Cabibbo M, Evangelista E, Spigarelli S, Vukcevic M (2003) Mater Sci Eng A 339:43
23. Gholamzadeh A, Karimi Taheri A (2009) Mech Res Commun 36:252
24. Liu XY, Pan QL, He YB, Li WB, Liang WJ, Min Z (2009) Mater Sci Eng A 500:150
25. Zhang H, Li L, Yuan D, Peng D (2007) Mater Charact 58:168
26. Dieter GE (1988) Mechanical metallurgy. SI Metric edition, London
27. Medina SF, Hernandez CA (1996) Acta Mater 44(1):137
28. Yang H, Li Z, Zhang Z (2006) J Zhejiang Univ Sci A 7(8):1453
29. Evangelista E, Forcellesa A, Gabrielli F, Mengucci P (1990) J Mater Process Technol 24:323
30. Chen ZY, Xu SQ, Dong XH (2008) Acta Metall Sin Engl Lett 21(6):451
31. Ward Flynn P, Mote J, Dorn JE (1961) Trans Met Soc AIME 221:1148
32. Takuda H, Fujimoto H, Hatta N (1998) J Mater Process Technol 80–81:513
33. Wang Y, Shao Z, Zhen L, Yang L, Zhang XM (2008) Mater Sci Eng A 497:479
34. Rønning B, Ryum N (2001) Metall Mater Trans A 32:769
35. Cerri E, Leo P, De Marco PP (2007) J Mater Process Technol 189:97
36. Mohamed AMA, Samuel FH, Samuel AM, Doty HW, Valtierra S (2008) Metall Mater Trans A 39:490
37. Kaiser MS, Datta S, Roychowdhury A, Banerjee MK (2008) J Mater Eng Perform 17(6):902
38. Mondolfo LF (1976) Aluminum alloys. Structure and properties. Butterworths, London
39. Prasad YVRK, Sasidhara S (1997) Hot working guide: a compendium of processing maps. ASM International, Materials Park, OH
40. Gandhi C (1982) Metall Trans A 13:1233
41. Styles CM, Sinclair I, Gregson PJ, Flitcroft SM (1994) Mater Sci Technol 10:475
42. Hardy HK, Heal TJ (1954) Progress in metal physics. Paragon Press, Oxford
43. Hirano K, Iwasaki H (1964) Trans Jpn Inst Met 5:162
44. Thompson DS (1969) Thermal analysis. Academic Press, New York
45. Zahra AM, Lafitte M (1974) Scripta Metall 8:165
46. Zahra AM, Zahra CY (1975) Scripta Metall 9:879
47. Papazian JM (1981) Metall Trans A 12:269
48. Jena AK, Gupta AK, Chaturvedi MC (1989) Acta Metall 37:885
49. Elagin VI (2007) Met Sci Heat Treat 49:427
50. Miao WF, Laughlin DE (2000) Metall Mater Trans A 31:361
51. Liu XY, Pan QL, Lu CG, He YB, Li WB, Liang WJ (2009) Mater Sci Eng A 525:128
52. Vietz JT, Polmear IJ (1966) J Inst Met 94(12):410
53. Hui-zhong L, Xin-ming Z, Ming-an C, Zhuo-ping Z (2006) J Cent S Univ Technol 13:130
54. Beffort O, Solenthaler C, Uggowitzer PJ, Speidel MO (1995) Mater Sci Eng A 191:121
55. Zakharov VV (2003) Met Sci Heat Treat 45:246
56. Emadi D, Whiting LV, Gertsman VY, Sahoo M (2002) AFS Trans 06–118:1